

Interaction of 28-GeV Protons with Uranium: Charge and Mass Distribution of Rare-Earth Products*

Y. Y. Chu, E. M. Franz, G. Friedlander, and P. J. Karol†

Chemistry Department, Brookhaven National Laboratory, Upton, New York 11973

(Received 6 July 1971)

Independent and cumulative yields of about 50 rare-earth nuclides produced in the interaction of 28-GeV protons with uranium have been measured. Chain yields on the neutron-excess side of β stability were found to have the same mass dependence as in low-energy fission. Based on the results obtained in the present study and with the aid of the published Cs isotopic distribution, charge-dispersion curves at $A \approx 147$ and $A \approx 170$ were constructed. The curve at $A \approx 147$ has two maxima, one on the neutron-deficient and one on the neutron-excess side of β stability, separated by a deep valley; the curve at $A \approx 170$ has a single peak on the neutron-deficient side of β stability. Corrections were made for feeding and depletion of various mass chains by α decay. Total isobaric yields were determined for 11 mass numbers between $A = 143$ and $A = 171$. On the basis of these results and published data at lower masses, a mass-yield curve was constructed. The apparent constancy of the neutron-deficient yields between mass 143 and mass 171 is consistent with the yield pattern of a spallation-like process. Over the mass range $50 < A < 160$, binary fission and spallation cannot account for all the observed yields. Other processes must be partially responsible for the production of these nuclides, especially at the lower masses.

I. INTRODUCTION

Interactions of uranium nuclei with protons in the GeV energy range have been the subject of a number of investigations by radiochemical, mass-spectrometric, track-detector, and counter-telescope techniques. In the present study cross sections for the formation of a large number of rare-earth nuclides in the interaction of 28-GeV protons with uranium were determined by radiochemical techniques in order to characterize the product distribution in charge and mass in the region $140 < A < 170$.

This work was undertaken because very little was known about formation cross sections for products with $A > 140$. In the mass region just below $A = 140$, a study in this laboratory¹ had revealed that the charge-dispersion (CD) curves are double-humped at proton energies of $\gtrsim 1$ GeV, with a valley near the line of β stability. This observation has been corroborated for the mass region $120 < A < 140$ by a number of investigators.²⁻⁶ At lower masses the CD curves were found to be somewhat asymmetric but without clear evidence of two maxima.⁵⁻¹⁴

The existence of two maxima in the CD curves suggested¹ that the dominant mechanisms responsible for the formation of neutron-excess products may differ from those giving rise to most of the neutron-deficient products. The neutron-excess species appeared to have all the characteristics of low-deposition-energy fission products, whereas the neutron-deficient products were interpreted

as resulting from events with higher deposition energies. Subsequent recoil studies^{2, 9, 15, 16} strengthened these conclusions. It should be noted, however, that the CD curves in the region $120 < A < 140$ have peak-to-valley ratios of only ~ 2 and that the two components cannot be cleanly resolved. It was thus clearly desirable to extend CD studies to higher masses, where the maxima might be more distinctly separable. Furthermore, CD data in different mass regions are needed for the construction of a mass-yield curve. The present study of rare-earth yields was therefore undertaken. Because of the complexity of the product mixtures it proved necessary to isolate many individual nuclides by a combination of chemical and mass separations.

While this research was in progress, another study of rare-earth nuclides produced in 28-GeV proton interactions with uranium was published.¹⁷ The latter work was done without mass separation, which may account for some of the discrepancies between the two sets of data (see Table II below).

II. EXPERIMENTAL

A. Irradiations

The irradiations, varying in length from 10 min to 3 h, were performed in the circulating proton beam of the Brookhaven alternating-gradient synchrotron. Approximately 10^{15} protons/min interacted in the target. Each target consisted of a 0.002-in.-thick uranium foil, cleaned in nitric acid and sandwiched between two stacks of three

0.001-in. aluminum foils. After irradiation, a $\frac{1}{2}$ -in.-diam circle was punched out of the foil stack. The uranium disk and the central aluminum disk of each of the two Al stacks were weighed in order to determine the relative numbers of uranium and aluminum nuclei irradiated. The ^{24}Na activity produced in these aluminum foils by the reaction $^{27}\text{Al}(p, 3pn)^{24}\text{Na}$ was later measured and served to monitor the proton beam intensity.

B. Chemical Separations

The uranium foil was dissolved in a small volume of concentrated HCl containing the appropriate rare-earth carriers. A few drops of concentrated HNO_3 were added and the mixture heated to ensure the complete dissolution and oxidation of the uranium. Separation of the rare earths from the U was accomplished by eluting the lanthanides through a Dowex 1 \times 8 column with 12 N HCl. The rare earths were further purified by a sequence of fluoride and hydroxide precipitations. Then one of two types of column procedures was used. In one case the rare-earth hydroxides were dissolved in dilute HCl, loaded onto a column of Dowex 50W \times 4 or \times 12 cation-exchange resin and eluted with α -hydroxyisobutyric acid. In the other case reversed-phase partition chromatography was used; the rare-earth hydroxides were dissolved in lactic acid, loaded onto a column packed with di-(2-ethyl hexyl)-orthophosphoric acid and siliconized kieselguhr, and eluted with HCl. The column size, resin specifications, concentration and pH of the eluent, rate of elution, and temperature were chosen for each experiment so as to optimize the separation of the particular rare earth being studied.

C. Mass Separations

For the mass separation the oxalate of the rare-earth group, or of the individual rare earth, was converted to the oxide by pyrolysis at 900°C and the oxide was introduced into the ion source of the Brookhaven electromagnetic isotope separator. A controlled stream of carbon tetrachloride vapor was allowed to pass through the heated sample to transform the oxides into volatile chlorides *in situ*. The chlorides were ionized inside the ion source and the ions accelerated and mass analyzed. The mass-separated samples were collected on 0.001-in.-thick pure aluminum foil at the empirically determined focal plane. The individual mass strips were mounted for radioactivity assay.

In order to measure the absolute cross sections it was necessary to determine the over-all yield of each product. When only chemical separations were performed, the yields of individual rare

earths in each sample were determined by x-ray fluorescence after completion of the radioactivity measurements. When mass separation followed chemical separation, the over-all yield of the element in question was determined by neutron activation analysis on an appropriate stable isotope (except in the case of Pm). The relative intensities of a suitable γ ray in sample and standard were compared by means of a Ge(Li) detector. The amounts of carriers used were chosen to avoid sputtering losses at the mass positions of the stable isotopes. This problem as well as possible mass-discrimination effects and other aspects of the isotope separation are discussed in Appendix A. Since promethium ($Z = 61$) does not have any stable isotopes, a known amount of ^{147}Pm tracer was added before the chemical and mass separations and the mass-separated 147 strip was finally assayed on a proportional counter to give the over-all yield of all the promethium isotopes.

D. Radioactivity Measurements

The radionuclides investigated are listed in Table I,¹⁸⁻³⁸ along with the specific radiations detected, their abundances, and the detection method used. Each sample was measured over a sufficient length of time to establish that it decayed with the proper half-life. The decay curves were analyzed by means of the CLSQ computer program³⁹ in order to obtain the end-of-bombardment or time-of-separation activities and their standard deviations.

The efficiency-vs-energy response curves of the Ge(Li) and NaI(Tl) γ -ray detectors were determined with National Bureau of Standards and International Atomic Energy Agency standards. The efficiencies of the thin NaI detectors for x rays were determined with calibrated sources⁴⁰ of ^{131}Cs and ^{241}Am . The efficiencies of the end-window proportional counters for β particles were taken from previous work in this laboratory. It is worth noting that, except for the cases of ^{169}Er and ^{170}Tm , all β measurements were done on essentially weightless samples resulting from the isotope separation and that the β end-point energies (again with the exception of ^{169}Er) are all >0.5 MeV. The efficiency of the Si α detector was determined with a calibrated ^{241}Am source.

III. RESULTS

The activities at end-of-bombardment or at separation time were converted to disintegration rates by use of the radiation abundances (given in Table I), counting efficiencies, and chemical yields. In addition, for many of the nuclides measured via x or γ rays, it was necessary to apply corrections

TABLE I. Relevant properties of nuclides measured. Unless otherwise noted, the properties were taken from Ref. 18.

Nuclide	Half-life	Radiation measured (keV)	Abundance	Method of detection ^a	Mass separation
¹⁴³ Ce	33 h	β	1.00	Prop.	+
¹⁴³ Pm	265 day	γ (742)	0.385 ^b	Ge, NaI	+
¹⁴⁴ Pm	365 day	γ (474)	0.45	Ge	+
		γ (615)	0.99	Ge	
		γ (696)	0.99	Ge	
¹⁴⁵ Sm	340 day	x ray	1.39	Thin NaI	
		γ (61)	0.13	Ge	
¹⁴⁵ Eu	5.93 day ^b	x ray	0.786 ^c	Thin NaI	+
		γ (654)	0.104 ^d	Ge, NaI	
		γ (894)	0.475 ^d	Ge, NaI	
¹⁴⁶ Pm	2020 day ^e	γ (453)	0.63 ^f	Ge, NaI	+
		γ (736)	0.23 ^f	Ge, NaI	
		γ (747)	0.36 ^f	Ge, NaI	
¹⁴⁶ Eu	4.65 day ^b	x ray	0.786 ^c	NaI	+
		γ (634)	0.77	Ge, NaI	
		γ (747)	1.00	Ge, NaI	
¹⁴⁶ Gd	48.27 day ^b			¹⁴⁶ Eu	+
¹⁴⁷ Nd	11.1 day	β	1.00	Prop.	+
		γ (91)	0.28	Ge	
¹⁴⁷ Eu	24 day	γ (122)	0.20	Ge	+
		γ (198)	0.24	Ge	
¹⁴⁷ Gd	38.06 h ^g	x ray	0.92 ^c	Thin NaI	+
¹⁴⁸ Pm	5.4 day	β	1.00	Prop..	+
^{148m} Pm	42 day	β	0.93	Prop.	+
		γ (550)	0.95	Ge	
¹⁴⁸ Eu	54 day	γ (550 + 553)	1.16 ^h	Ge	+
		γ (630)	0.71 ^h	Ge	
¹⁴⁸ Gd	84 yr	α (3180)	1.00	Si	+
¹⁴⁹ Nd	1.73 h ⁱ	β	1.00	Prop.	+
		γ (114)	0.18	Ge	
				¹⁴⁹ Pm	
¹⁴⁹ Pm	53.1 h	β	1.00	Prop.	+
		γ (286)	0.026 ^b	Ge	
¹⁴⁹ Eu	93.1 day ^b	x ray	0.765 ^c	Thin NaI	+
		γ (277)	0.0336 ^b	Ge	
		γ (328)	0.0391 ^b	Ge	
¹⁴⁹ Gd	9.25 day ^b	γ (150)	0.48	Ge	+
^{149m} Tb	4.1 h	α (3990)	0.226 ^d	Si	+
¹⁵⁰ Pm	2.7 h	β	1.00	Prop.	+
		γ (334)	0.71	Ge	
¹⁵⁰ Eu	12.6 h	β	0.90	Prop.	+
^{150m} Eu	5 yr	x ray	0.77 ^c	Thin NaI	+
¹⁵¹ Pm	28 h	β	1.00	Prop.	+
		γ (340)	0.21	Ge	
¹⁵¹ Gd	120 day	γ (154)	0.0577 ^j	Ge	+
		γ (175)	0.0273 ^j	Ge	
¹⁵¹ Tb	18 h	γ (108)	0.35	Ge	+
		γ (252)	0.35	Ge	
		γ (288)	0.32	Ge	
¹⁵² Eu	12.7 yr	β	0.28	WL Prop.	+
^{152m} Eu	9.3 h	β	0.77	Prop.	+
¹⁵³ Sm	46.8 h	β	1.00	Prop.	+
		γ (103)	0.28	Ge	
¹⁵³ Tb	56.2 h ^b	x ray	1.040	NaI	+
		γ (212)	0.30	Ge	
				¹⁵³ Gd	
¹⁵⁶ Sm	9.4 h	β	1.00	Prop.	+
¹⁵⁶ Eu	15.4 day	β	1.00	Prop.	+

TABLE I (Continued)

Nuclide	Half-life	Radiation measured (keV)	Abundance	Method of detection ^a	Mass separation
¹⁵⁷ Eu	15.2 h	β	1.00	Prop.	+
		γ (64)	0.186 ^k	Ge	
¹⁵⁹ Gd	18 h	γ (413)	0.23 ^k	Ge	+
		β	1.00	Prop.	
¹⁶¹ Tb	6.9 day	β	1.00	Prop.	+
¹⁶⁵ Er	10.3 h	x ray	0.76	Thin NaI	+
¹⁶⁵ Tm	30.1 h	γ (243)	0.45 ^l	Ge	+
¹⁶⁶ Tm	7.7 h	γ (184)	0.168 ^m	Ge	+
¹⁶⁸ Yb	56.7 h ⁿ			¹⁶⁸ Tm	+
¹⁶⁷ Tm	9.25 day ⁿ	γ (208)	0.43	Ge	+
¹⁶⁸ Tm	93.1 day ^o	γ (80)	0.115 ^p	Ge	
		γ (184)	0.17 ^p	Ge	
		γ (198)	0.52 ^p	Ge	
		β	1.0	Prop.	
¹⁶⁹ Er	9.4 day	β	1.0	Prop.	
¹⁶⁹ Yb	31.8 day	γ (198)	0.35	Ge	
¹⁶⁹ Lu	34 h	γ (191)	0.17 ^q	Ge	+
		γ (965)	0.20 ^q	Ge	
¹⁷⁰ Tm	128.6 day ^r	β	1.00	Prop.	
		γ (84)	0.033	Ge	
¹⁷⁰ Lu	2.05 day	γ (84)	0.095 ^s	Ge	+
¹⁷⁰ Hf	15.92 h ^t			¹⁷⁰ Lu	
¹⁷¹ Lu	8.22 day ⁿ	γ (741)	0.46 ^u	Ge	+
¹⁷¹ Hf	12.1 h ^t			¹⁷¹ Lu	
¹⁷² Lu	6.7 day	γ (182)	0.22 ^v	Ge	
		γ (810)	0.15 ^v	Ge	
		γ (901)	0.29 ^v	Ge	
		γ (1095)	0.67 ^v	Ge	

^a The symbols used in this column have the following meanings: Prop., end-window flow proportional counter; WL Prop., windowless proportional counter; Ge, Ge(Li) detector; NaI, 3-in. \times 3-in. NaI(Tl) detector; thin NaI, 2-mm-thick NaI(Tl) detector; Si, silicon surface-barrier detector; when a nuclide was detected via the radiations of its radioactive daughter, the symbol of the daughter is listed.

^b Reference 19.

^c Reference 18; appendixes.

^d Reference 20.

^e Reference 21.

^f Reference 22.

^g Reference 23.

^h Reference 24.

ⁱ Reference 25.

^j Reference 26.

^k Reference 27.

^l Reference 28.

^m Reference 29.

ⁿ Reference 30.

^o Reference 31.

^p Reference 32.

^q Reference 33.

^r Reference 34.

^s Reference 35.

^t Reference 36.

^u Reference 37.

^v Reference 38.

for loss of counting rate in the photopeak due to summing with coincident radiation (particularly important for the summing with K x rays). These corrections, determined with the aid of photopeak- and total-efficiency curves for the detectors used, required detailed consideration of the decay schemes. Most of the correction factors turned out to be between 1.00 and 1.10, but in a few instances the factors were as large as 1.3.

Cross sections were obtained from the disintegration rates at separation or end-of-bombardment time in the manner described in Ref. 1.

For the cross section of the monitor reaction $^{27}\text{Al}(p, 3pn)^{24}\text{Na}$, the value 8.6 mb taken from Cumming's⁴¹ smoothed excitation function was used. To calculate cross sections for the independent formation of nonshielded nuclides, corrections for growth and decay during irradiation and up to the time of parent-daughter separation were applied as in Ref. 1. The effective separation time for column separation procedures was obtained by a method described elsewhere.⁴²

Corrections for losses from the target foil by recoil were estimated from Bächman's data¹⁷ to

be 1.5% for neutron-deficient and 4.0% for neutron-excess products. These values were used over our entire mass range, although the corrections should probably be even smaller at the high-mass end.

The contributions to measured activities from low-energy secondaries produced in the target had to be taken into account. The only products for which these contributions are significant are the ^{24}Na in the Al monitors and the neutron-excess fission products. In a separate experiment⁴³ the ^{24}Na production by secondaries was determined by measurement of the $^{18}\text{F}/^{24}\text{Na}$ ratio in a standard Al-U-Al foil stack as compared with the same ratio in a pure Al stack. The data indicate a secondary contribution of ~13% to ^{24}Na production from 100 mg/cm² of U target, approximately three times the effect at 3-GeV proton energy.⁴⁴ In another series of experiments,⁴³ the corrections for the neutron-excess fission products produced by low-energy secondaries were determined. Based on the assumption that secondary effects are negligible for neutron-deficient products, yield ratios of neutron-excess to neutron-deficient nuclide pairs from five elements (Sr, Pd, Ba, Nd, Sm) were measured for three different thicknesses of uranium targets bombarded with 28-GeV protons. The secondary effect was found to increase with mass of the product up to $A \approx 140$, but to be approximately constant at ~30% per 100 mg/cm² in the Ba to Sm region. Under the assumption that this effect is linear with target thickness, corrections of ~25% were therefore applied to the cross sections for all the neutron-excess products in the rare-earth region.

The uncertainty (standard deviation) to be assigned to each cross-section measurement was arrived at by root-mean-square combination of the various individual sources of error (even though some of them may be systematic rather than random), which are as follows: counting statistics and decay curve analysis (mostly <5%, in a few instances up to 25%); counting efficiencies (5-10%); photopeak summing correction (uncertainty estimated as 25% of the correction, i.e., 0-7%); chemical yield determinations (3-5%); secondary contribution to ^{24}Na in monitor (2%); secondary contribution to neutron-excess yields (5%); recoil loss (1-2%); separation-time uncertainty (0-15%).

When several determinations of a cross section were made, the weighted average was obtained by weighting each individual value by the inverse square of its assigned standard deviation σ_i . These weighted average cross sections are listed in Table II, column 4. The uncertainty shown is either the average deviation Δ of the individual results

from the weighted average or the value σ obtained from $1/\sigma^2 = \sum (1/\sigma_i^2)$, whichever is larger. When only a single determination was done, its σ_i value is given. The number of determinations is shown in column 6. Column 2 identifies each cross section as independent (I) or cumulative (C). In column 3 the distance from the line of β stability along an isobaric chain ($Z_A - Z$) is given for each product. The manner in which the Z_A values were chosen is discussed in Sec. IV below and in Appendix B.

In the last column of Table II, the measured cross sections from Ref. 17 are listed for comparison. The ratios of the cross sections determined in the present work to those reported in Ref. 17 range from 0.3 to 8.5, and for 9 out of the 21 nuclides determined in both studies the two values differ by more than a factor 2. In view of these discrepancies it is remarkable that Bächmann¹⁷ was able to arrive at conclusions about CD and mass-yield curves that are at least qualitatively similar to those reached on the basis of the present data.

IV. DISCUSSION

For a complete description of the yield surface in a given region of A and Z one needs to know the independent formation cross section of every nuclide in that region. Such information is, of course, not available from the present study in the rare-earth region. Nevertheless, under the assumption that the yield surface is smooth, its major features will be deduced from the data at hand by considering cuts through the surface along lines of constant A (CD curves).

Charge Dispersion

A CD curve is defined as a plot of cross sections for independent formation of the isobars at a given A vs atomic number Z (or some function of Z).

In practice, it is rarely possible to obtain a sufficient number of independent formation cross sections for complete delineation of CD. As in previous investigations^{1,7} we therefore (a) combined results from several neighboring mass chains and (b) used cumulative yields to aid in delineating the distributions.

In order to combine cross-section data from several mass chains into a single CD curve it is necessary to make corrections for any mass-yield variations. Our approach will be to use published mass-yield data as a starting point. Once the CD curves in several mass regions have been constructed, they will then be used to obtain improved mass-yield data.

TABLE II. Summary of measured cross sections.

Nuclide	Type of yield ^a	$Z_A - Z$	Cross section (mb)	Type of error	Number of determinations	Previous results ^b
¹⁴³ Ce	C	+2.27	7.07 ± 0.92	σ	1	6.8 ± 0.5
¹⁴³ Pm	C	-1.63	4.68 ± 0.42	σ	1	0.55 ± 0.05
¹⁴⁴ Pm	I	-1.31	0.55 ± 0.03	σ	2	
¹⁴⁵ Sm	I	-1.66	0.93 ± 0.08	σ	4	
¹⁴⁵ Eu	C	-2.71	5.93 ± 0.83 ^c	Δ	5	4.00 ± 0.35
¹⁴⁶ Pm	I	+0.37	0.37 ± 0.07	Δ	2	
¹⁴⁶ Eu	I	-2.15	1.45 ± 0.34	Δ	2	0.87 ± 0.07
¹⁴⁶ Gd	C	-3.38	5.17 ± 0.34	Δ	2	5.06 ± 0.40
¹⁴⁷ Nd	C	+1.57	3.31 ± 0.29	Δ	3	1.7 ± 0.17
¹⁴⁷ Eu	I	-1.79	1.11 ± 0.15	Δ	5	0.30 ± 0.03
¹⁴⁷ Gd	C	-2.74	4.74 ± 0.50	Δ	4	3.05 ± 0.25
¹⁴⁸ Pm	I	+0.87	0.0154 ± 0.0047	Δ	2	0.004 ± 0.001
^{148m} Pm	I	+0.87	0.221 ± 0.022	σ	2	0.17 ± 0.02
¹⁴⁸ Eu	I	-1.13	0.66 ± 0.03	σ	3	0.48 ± 0.10
¹⁴⁸ Gd	C	-2.38	7.08 ± 0.78	σ	1	
¹⁴⁹ Nd	C	+2.12	1.93 ± 0.15	σ	1	
¹⁴⁹ Pm	C	+1.12	2.04 ± 0.34	Δ	5	0.48 ± 0.05
¹⁴⁹ Pm	I	+1.12	0.347 ± 0.112	Δ	2	
¹⁴⁹ Eu	I	-0.88	0.56 ± 0.05	Δ	3	0.08 ± 0.02
¹⁴⁹ Gd	C	-1.89	6.46 ± 0.95 ^c	Δ	5	
^{149m} Tb	C	-3.09	1.75 ± 0.14 ^c	σ	2	3.60 ± 0.8
¹⁵⁰ Pm	I	+1.44	0.193 ± 0.015	σ	1	
¹⁵⁰ Eu	I	-0.56	0.0074 ± 0.0011	σ	1	0.02 ± 0.05
^{150m} Eu	I	-0.56	≤ 0.034		1	
¹⁵¹ Pm	C	+1.67	0.85 ± 0.10	Δ	3	0.24 ± 0.04
¹⁵¹ Gd	I	-1.33	1.23 ± 0.12	σ	2	
¹⁵¹ Tb	C	-2.33	3.36 ± 0.22	Δ	2	4.51 ± 0.5
¹⁵² Eu	I	-0.04	≤ 0.38		1	
^{152m} Eu	I	-0.04	0.028 ± 0.003	σ	1	
¹⁵³ Sm	C	+1.23	0.53 ± 0.053	Δ	4	0.46 ± 0.08
¹⁵³ Tb	C	-1.77	6.15 ± 0.44	Δ	2	
¹⁵⁶ Sm	C	+2.20	0.130 ± 0.049	Δ	2	0.22 ± 0.05
¹⁵⁶ Eu	I	+1.16	0.090 ± 0.021	σ	2	0.28 ± 0.04
¹⁵⁷ Eu	C	+1.52	0.106 ± 0.017	Δ	2	0.20 ± 0.03
¹⁵⁹ Gd	C	+1.21	0.064 ± 0.009	σ	1	
¹⁶¹ Tb	C	+0.91	0.054 ± 0.007	σ	1	
¹⁶⁵ Er	I	-0.65	0.063 ± 0.046	σ	1	
¹⁶⁵ Tm	C	-1.65	4.70 ± 0.26	Δ	4	
¹⁶⁶ Tm	I	-1.27	0.142 ± 0.046	σ	1	
¹⁶⁶ Yb	C	-2.30	4.91 ± 0.48	Δ	3	
¹⁶⁷ Tm	C	-0.93	5.83 ± 0.55	Δ	7	
¹⁶⁸ Tm	I	-0.55	0.036 ± 0.0055	Δ	2	
¹⁶⁹ Er	C	+0.78	0.0044 ± 0.0016	Δ	3	
¹⁶⁹ Yb	C	-1.22	6.88 ± 0.47	σ	1	
¹⁶⁹ Lu	C	-2.22	6.82 ± 0.41	σ	3	
¹⁷⁰ Tm	I	+0.16	0.0075 ± 0.0020	Δ	2	
¹⁷⁰ Lu	I	-1.84	0.544 ± 0.089 ^d		3	
¹⁷⁰ Hf	C	-2.87	4.48 ± 0.52 ^d		3	
¹⁷¹ Lu	I	-1.50	0.034 ± 0.041 ^d		5	
¹⁷¹ Hf	C	-2.50	6.50 ± 0.50 ^d		5	
¹⁷² Lu	I	-1.11	0.079 ± 0.022	Δ	3	

^a C denotes cumulative yield, I denotes independent yield.

^b Reference 17. Note that Bächmann's cross sections for Pm are only relative.

^c The ¹⁴⁵Eu cumulative yield given was obtained by subtracting from the measured yield the contribution of the ^{149m}Tb α branch. The ¹⁴⁹Gd cumulative yield quoted includes the ^{149m}Tb cumulative yield. The 4-min ^{149g}Tb decays 99.97% by electron capture to ¹⁴⁹Gd.

^d Both the cross sections and errors for the ¹⁷⁰Lu-¹⁷⁰Hf and ¹⁷¹Lu-¹⁷¹Hf pairs were derived from data taken on several Lu samples with various Lu-Hf chemical separation times by using the weighted least-squares technique.

Figure 1 is a mass-yield curve for interaction of uranium with 28-GeV protons constructed from published data.^{8, 11, 17} Although some of the final results for mass-yield values in the rare-earth region arrived at in this paper differ substantially from those given by Bächmann¹⁷ (see next section), this has little effect on the over-all shape of the curve and is of negligible consequence for the mass corrections to the CD curves.

As will become apparent in the discussion of the $A = 147$ CD curve, it is important to know the mass dependence not only of total formation cross sections, but also of the contributions on the neutron-excess and neutron-deficient sides of β stability. Our data for cumulative cross sections on the neutron-excess side are shown in Fig. 2. They drop off very rapidly with increasing A , in very much the same manner as the cumulative yields obtained in fission of uranium by low-energy particles.^{45, 46} The decrease in neutron-excess cumulative yields from $A = 143$ to $A = 150$ (the range used for the construction of our CD curve at $A = 147$) completely accounts for the drop in the total mass yields (Fig. 1). Thus the neutron-deficient yields in this region are virtually constant with A .

In the region $165 \leq A \leq 172$ (used for construction of a CD curve at $A = 170$) the yields of neutron-excess products (Fig. 2) contribute negligibly to the total yields, and the yields of neutron-deficient products show no significant variation with mass (cf. Table II). No mass-yield corrections are therefore necessary in the construction of this CD curve.

A further problem that arises in constructing CD curves from data spanning several mass numbers is the choice of an appropriate abscissa. In previous papers on charge dispersion^{1, 7} N/Z has been used. As pointed out by Hogan and Sugarman,⁴⁷ this can lead to distortions of the curves

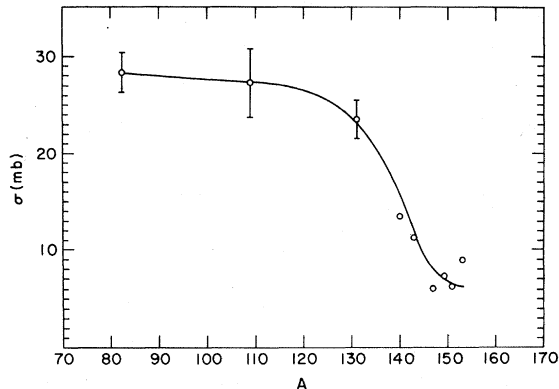


FIG. 1. Portion of mass-yield curve for the interaction of 28-GeV protons with uranium based on published data (Refs. 8, 11, 17).

when data from several mass chains are used. Also, as will be shown, shell structure may have a significant effect on the shapes of CD curves in the rare-earth region, and N/Z is not a suitable parameter for displaying such effects. In the present paper all CD curves are therefore plotted with $Z_A - Z$ as the abscissa, where Z_A is the Z value at the minimum of the appropriate mass parabola for mass number A . The $Z_A - Z$ values were obtained from the mass table of Garvey *et al.*⁴⁸ in a manner described in Appendix B.

The cross sections for products with $143 \leq A \leq 150$ and $165 \leq A \leq 172$ listed in Table II were used to construct CD curves for $A = 147$ and $A = 170$. The data in the 147 region are shown in Fig. 3. The open circles represent the independent-formation cross sections, filled circles the cumulative ones. According to the above discussion, neutron-excess yields for $A > 147$ must all be increased by applying the A dependence of neutron-excess cumulative yields illustrated in Fig. 2. The resulting cross sections are shown as open squares in Fig. 3. No such readjustment is required for independent-production cross sections of neutron-deficient nuclei with $A \neq 147$ in the range 143–150, since the neutron-deficient cumulative

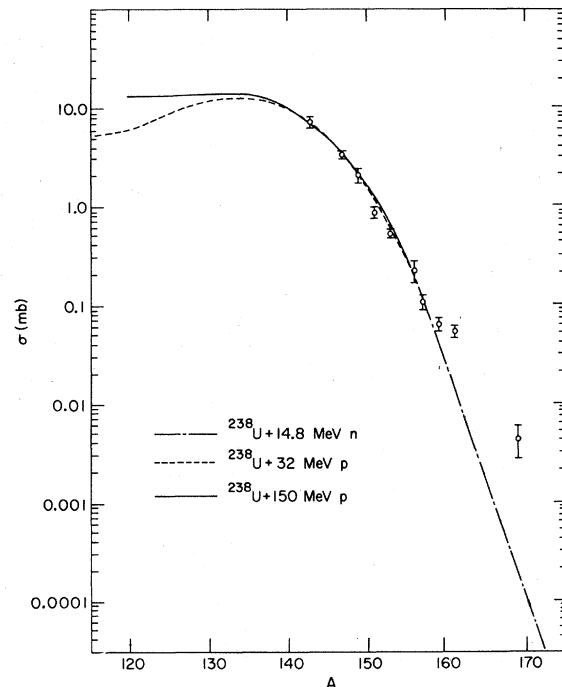


FIG. 2. Cumulative yields of the neutron-excess rare-earth nuclides. The points are measured values from this work. The dash-and-dot curve is from 14-MeV neutron fission of uranium (Ref. 45). The dashed and the solid curves are from 32- and 150-MeV proton fission of uranium, respectively (Ref. 46). All three curves are normalized at the measured $A = 147$ point.

yields are essentially independent of A as described earlier.

As seen in Fig. 3, even the entire ensemble of measured independent yields over the mass range 144–150 defines only the central region of the CD curve. The magnitudes of the cumulative yields make it clear, however, that there must be maxima on both sides of the valley near $Z = Z_A$ defined by the independent yields. Unfortunately the shapes and positions of these peaks cannot be uniquely determined from the cumulative yields. Data on independent yields far from β stability would be highly desirable for this purpose, but such data are not presently accessible in the rare-earth region.

The most complete set of independent-formation cross sections including those far from β stability was obtained by Chaumont,⁶ who used on-line mass spectrometry to measure the isotopic distributions of Cs and Rb nuclides formed in 24-GeV proton interactions with U. These data are shown in Fig. 4. The heaviest Cs isotope measured, ¹⁴⁴Cs, is in the mass region under discussion and will be used to help define the neutron-excess wing of the $A = 147$ CD curve. Furthermore the rates of drop-off on the far wings of the Rb and Cs distributions are so rapid and so nearly the same that they can presumably serve as a guide for the rate of drop-off in the rare-earth region also. For this purpose the Cs isotopic distribution must be transformed into a CD (or isobaric distribution) by changing the ab-

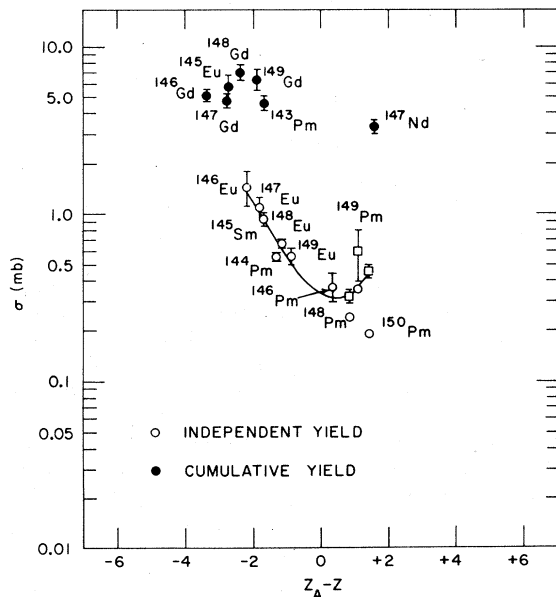


FIG. 3. Independent and cumulative yields for the mass range $143 \leq A \leq 150$. The open squares for ^{148,149,150}Pm have been corrected to $A = 147$ for mass-yield variation, as discussed in the text. The $Z_A - Z$ values at which points are plotted are the $Z_A - Z_{\text{eff}}$ values discussed in Appendix B.

scissa from A to $Z_A - Z$ and making the appropriate corrections for mass-yield variation in the A range 119 to 144. The procedure is described in detail in Appendix C and the resulting "CD curve at $A = 131$ " is shown in Fig. 5. The two curves plotted are based on two quite different sets of mass-yield corrections discussed in the Appendix. As is evident from Fig. 5, the shapes of the wings are quite insensitive to the details of these corrections. (This is not surprising since the drop-off at the wings is determined by only three or four neighboring mass points.) The "CD curve at $A = 131$ " in Fig. 5 differs substantially from the one previously inferred from much more limited data.⁷ In particular, the new curve has an appreciably steeper slope on the far neutron-deficient side. In addition, the effect of the $N = 82$ shell (which is reflected in the $Z_A - Z$, but not in the N/Z representation) leads to a shift of the neutron-excess peak to the right in Fig. 5, as compared to the curve of Ref. 7.

We can now proceed to complete the construction of the CD curve at $A = 147$. In Fig. 6 the central portion of the curve is identical with that in Fig. 3, but the data points are omitted for clarity. With the aid of the independent yield of ¹⁴⁴Cs from Chaumont⁶ (corrected to $A = 147$ by means of the mass-yield curve in Fig. 2), the ¹⁴⁷Nd cumulative yield (which includes σ_{ind} for ¹⁴⁷Nd and for all its precursors, ¹⁴⁷Pr, ¹⁴⁷Ce, ¹⁴⁷La, etc.), and the

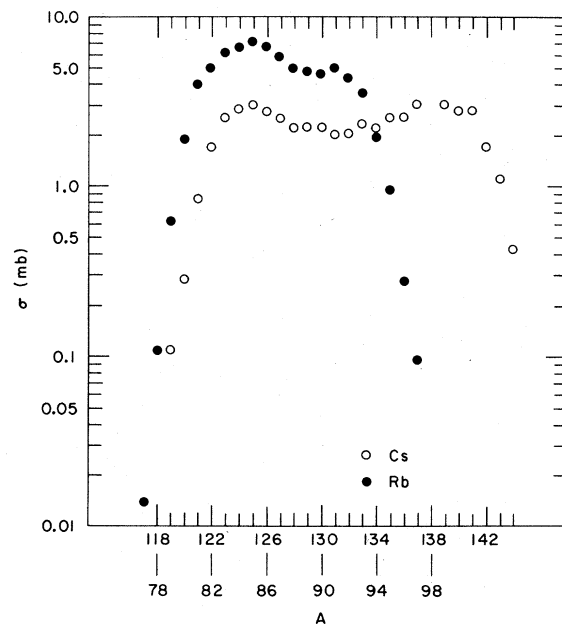


FIG. 4. Isotopic distributions of Cs and Rb from the interaction of 24-GeV protons with uranium (Ref. 6). The upper mass scale is for Cs isotopes, and the lower for Rb isotopes.

rate of drop-off beyond $Z_A - Z \approx 4.5$ taken from Fig. 5, the neutron-excess branch of the curve is uniquely determined as shown in Fig. 6.

On the neutron-deficient side, there are significant α branches for nuclides with $N=84$ and 85 and they affect a number of the neutron-deficient cumulative yields in this mass range. With the exception of ^{149m}Tb , no α emitters have been directly measured in this work, because of their relatively short half-lives. In order to estimate the magnitudes of these α contributions, a CD curve had to be constructed first based on the measured but uncorrected cumulative yields. The dashed curve in Fig. 6 gives the best fit to these values, with the slope on the far wing taken from Fig. 5. The first estimate of α contributions to four gadolinium cumulative yields using this CD curve is given in column 6 of Table III. A second CD curve, based on these corrected cumulative yields, is indicated as dashed-and-dot curve in Fig. 6. The second estimate of α contributions using the dashed-and-dot curve is listed in column 7 of Table III. A third iteration led to satisfactory convergence. The final α corrections are given in column 8 and the corrected cumulative yields in the last column. The solid curve in Fig. 6 represents the final corrected CD curve for $A=147$.

The independent and cumulative yields obtained in the region $165 \leq A \leq 172$ are displayed in Fig. 7. As expected from Fig. 2, the yields on the neutron-excess side of β stability are extremely low.

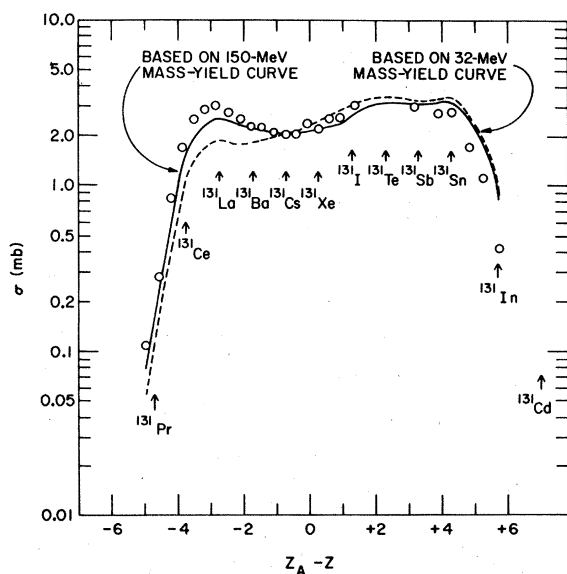


FIG. 5. Charge-dispersion curve for $A=131$ derived from the Cs isotopic distribution from the interaction of 24-GeV protons with uranium (Ref. 6). See detailed description in Appendix C. The abscissa is $Z_A - Z_{\text{eff}}$ as described in Appendix B.

Based on the cumulative yield of ^{169}Er , one can set an upper limit of about $5 \mu\text{b}$ for any neutron-excess contribution to the CD in this mass region.

As mentioned earlier, no mass-yield correction was applied to the data in this mass region. The CD curve is nominally designated as applying at $A=170$. The same procedure adopted for the construction of the $A=147$ CD curve was used. The slope on the far neutron-deficient side was again taken from Fig. 5 and the height and width of the peak were fitted to the seven measured cumulative yields. The result is the solid curve shown in Fig. 8. No corrections for α contributions were made because all known α emitters in the heavier mass range are at least six charge units away from the β -stability line, and their contributions are therefore not significant. The solid curve in Fig. 8 gives the best fit to the experimental points and the two dashed curves delineate the band of pos-

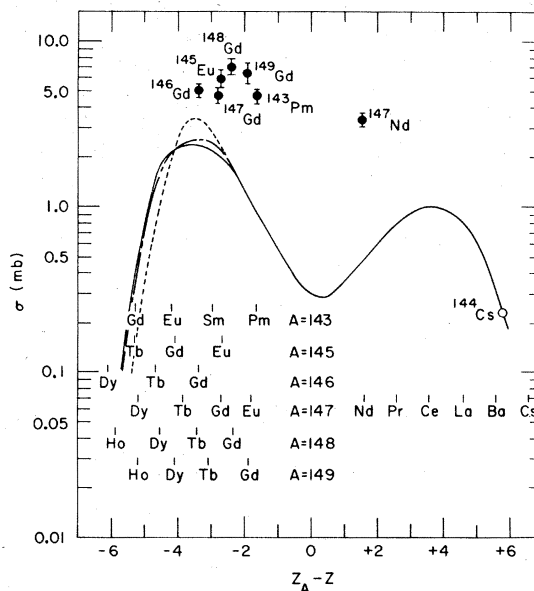


FIG. 6. Charge-dispersion curve for $A=147$. The independent yield of ^{144}Cs is taken from Ref. 6 (corrected for the mass difference). The dashed curve was drawn to match the measured cumulative yields. The dash-and-dot and solid curves represent the successive approximations obtained when α decay was taken into account. The solid curve was drawn so that the sum of the isobaric yields reads off the curve approximate the final corrected cumulative yields measured in this work.

Nuclide	$\sigma_{\text{exp}} (\text{CORR})$ (mb)	σ_{curve} (mb)
^{143}Pm	4.68 ± 0.42	5.55
^{145}Eu	5.93 ± 0.83	4.52
^{146}Gd	4.46 ± 0.34	3.80
^{147}Nd	3.31 ± 0.29	3.31
^{147}Gd	3.94 ± 0.50	4.74
^{148}Gd	5.94 ± 0.78	5.90
^{149}Gd	5.58 ± 0.95	6.00

as these curves might suggest. There is a narrow band around each curve encompassing possible solutions as shown in Fig. 8. For all practical purposes, the neutron-deficient peaks for these two mass regions are quite similar, although their positions on a $Z_A - Z$ scale appear to be significantly different from that of the peak for $A \approx 131$. The rapid decrease of cumulative yields with increasing mass shown in Fig. 2 is clearly reflected in the vast difference in the neutron-excess wings. In short, the CD curve changes from a double hump with shallow valley in between (peak-to-valley ratio < 2) at $A \approx 131$ to a distinct separation of two maxima (peak-to-valley ratio ~ 8) at $A \approx 147$ to a single peak on the neutron-deficient side at $A \approx 170$. The CD curve at $A \approx 147$ shows the most pronounced separation of the neutron-deficient branch from the neutron-excess branch in a CD curve observed to date.

Mass-Yield Curve

A number of isobaric yields were evaluated based on the results obtained in the present study. In addition to the measured independent and cumulative yields corrected for α contributions or α depletions (see Table III), other independent yields were needed in some mass chains to give the total isobaric yields. However, in most of these chains, the measured cross sections represent more than 90% of the total isobaric yield. For example, at

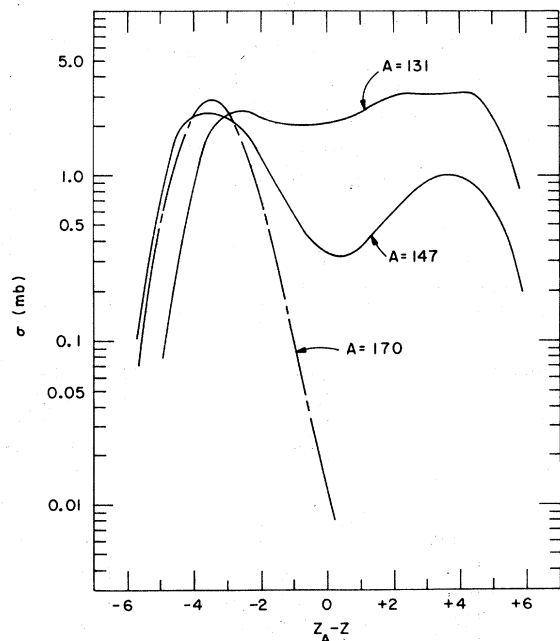


FIG. 9. Charge-dispersion curves for $A \approx 131$, $A \approx 147$, and $A \approx 170$. The abscissa is $Z_A - Z_{\text{eff}}$ as discussed in Appendix B.

$A = 147$, only the independent yields of ^{147}Pm and ^{147}Sm were not measured. From Fig. 3 these are found to be 0.44 and 0.30 mb, respectively. Together with the measured independent yield of ^{147}Eu and the cumulative yields of ^{147}Nd and ^{147}Gd (the latter corrected for α feeding) these values lead to a total isobaric yield of 9.1 ± 1.0 mb.

For mass chains other than 131, 147, and 170, interpolation between data at two of these masses was necessary. For nuclides on the neutron-excess side of the valley, this was done with the aid of Fig. 2, for others by means of the CD curves of Fig. 9. For example at $A = 151$, the yield of ^{151}Sm was estimated as follows: The value corresponding to the $Z_A - Z_{\text{eff}}$ of ^{151}Sm was read off the $A = 147$ CD curve (Fig. 6) and was corrected for the mass difference between 147 and 151 by the neutron-excess mass-yield curve in Fig. 2. The ^{151}Eu yield was obtained by linear interpolation between the $A = 147$ and $A = 170$ CD curves (Fig. 9) at the appropriate $Z_A - Z_{\text{eff}}$ value. As seen in Table IV, these two interpolated yields contribute only 0.38 mb to the total isobaric yield of 6.62 ± 0.50 mb for $A = 151$. The same procedure was used at $A = 143$, 149, and 153, with the nonmeasured yields contributing 13, 3, and 5%, respectively, to the total isobaric yields.

For $A \geq 165$, no mass-yield corrections were made in estimating the missing independent yields. These cross-section values were read off directly from the $A \approx 170$ CD curve, and they amount to only 1% or less of the isobaric chain yields.

The new data for isobaric yields, together with literature values for other mass regions, are listed in Table V. In Fig. 10, a new mass-yield curve for the interaction of 28-GeV protons with uranium is drawn on the basis of these data (solid curve). For comparison, the portion of the mass-yield curve based on literature values alone (Fig. 1) is

TABLE IV. Measured and interpolated cross sections at $A = 151$.

Nuclide	Type of yield ^a	$Z_A - Z_{\text{eff}}$	σ (mb) ^b
^{151}Pm	C		0.85
^{151}Sm	I	+0.67	(0.09)
^{151}Eu	I	-0.33	(0.29)
^{151}Gd	I		1.23
^{151}Tb	C		4.16 ^c

^a C denotes cumulative yield, I denotes independent yield.

^b Values in parentheses are interpolated, the others are measured.

^c 0.8 mb has been added to the measured value of 3.36 mb to take account of α depletion of ^{151}Dy and ^{151}Ho (see Table III).

shown also as the long-dashed curve. The two curves differ very little and only for $A \lesssim 137$. Since the only direct use made of the curve of Fig. 1 was in the transformation of the Cs isotopic distribution to a "CD curve at $A = 131$ " and there only for $131 \leq A \leq 137$ (see Appendix C), the results would not have been different if the new mass-yield data had been used.

The rather pronounced structure of the mass-yield curve makes it tempting to discuss it in terms of reaction mechanisms that may contribute to the yields in different mass regions. The broad peak in the region $50 < A < 160$ is almost certainly associated with a binary-fission process. From measurements with mica track detectors⁴⁹ the binary-fission cross section of uranium with 29-GeV protons is known to be 668 ± 34 mb. Although the mass distribution in binary fission of uranium has not been measured at this energy, it is safe to assume that it is essentially confined to the region $50 < A < 160$ as has been established by counter coincidence measurements at 2.9-GeV bombarding energy.⁵⁰ The integrated area under the curve of Fig. 10 over this mass range is 2.25 ± 0.15 b. Subtracting twice the binary-fission cross section from this value leaves 0.91 ± 0.15 b to be accounted for by other processes.

It turns out, perhaps somewhat fortuitously, that the trapezoidal area bounded by the dot-dashed lines in Fig. 10 corresponds to a cross section of

TABLE V. Isobaric cross sections for the interaction of 28-GeV protons with uranium.

Mass number	Cross section (mb)	Reference
21	38 \pm 3	a
38	15.3 \pm 1.0	a
48	14.9 \pm 1.5	b
72	16.5 \pm 1.7	c
83	28.3 \pm 2.0	a
109	27.2 \pm 3.5	d
131	23.5 \pm 2	a
143	13.5 \pm 1.5	e
147	9.1 \pm 1.0	e
149	8.4 \pm 1.4	e
151	6.6 \pm 0.5	e
153	8.0 \pm 0.6	e
165	4.8 \pm 0.3	e
166	5.1 \pm 0.5	e
167	5.8 \pm 0.6	e
169	6.9 \pm 0.5	e
170	5.1 \pm 0.6	e
171	6.6 \pm 0.6	e

^a Reference 11.

^b Y. Y. Chu, unpublished, quoted in Ref. 7.

^c S. Kaufman, unpublished, quoted in Ref. 7.

^d Reference 8.

^e This work.

1.04 b, while the short-dashed curve, which represents the difference between the solid curve and the dot-dashed line, encompasses 1.21 b or very nearly twice the binary-fission cross section obtained with the mica technique.⁴⁹ Whether or not the dashed curve is an exact representation of the binary-fission yields, it cannot be grossly different, and the conclusion is inescapable that the over-all contribution to the mass range in question from processes other than those registered as binary events in mica is about 1 b and decreases with increasing A .

The products in the region of $A \approx 170$, with cross sections of 5 to 7 mb per mass number, may well be principally formed as spallation residues. According to the general trends of spallation yields of products far removed from the target,⁵¹ one would expect the spallation yields to drop or at most stay constant with decreasing mass number. This expectation is borne out by the essential constancy of the chain yields on the neutron-deficient side observed in the range $147 < A < 170$. A flat distribution of spallation yields over the entire range would account for ≈ 0.5 b between $A = 50$ and $A = 160$, leaving another 0.5 b to be ascribed to other mechanisms. More likely the contributions of processes other than those mentioned above should be even larger.

It is worth noting that the cross section for production of single, unpaired tracks in mica due to the interaction of 29-GeV protons with U was found to be 0.30 b.⁴⁹ Some fraction of the 0.30 b is very likely due not to spallation but to binary fission with one partner below the recording threshold in mica (as was found to be the case for most of the single tracks at 3 GeV⁴⁹). The true cross section for binary fission would then be somewhat larger

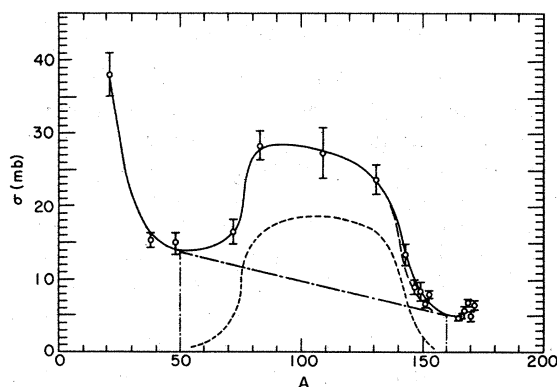


FIG. 10. Mass-yield curve of 28-GeV protons interacting with uranium. The long-dashed curve between mass 137 and mass 153 corresponds to the mass-yield curve from the same mass region in Fig. 1. The meanings of the short-dashed curve and the dot-dashed lines can be found in the text.

than the measured 668 mb. The mass-yield distribution for processes other than binary fission may then very well have a minimum or a depression in the fission peak region rather than a monotonic decrease with increasing A .

It might be pointed out that the situation encountered here is not peculiar to uranium. In the interactions of high-energy protons with lighter elements, where fission at very low deposition energies cannot occur, analysis of the mass-yield curve into different high-deposition-energy mechanisms may in fact be more clear-cut. Sufficient information is not available at ~ 28 -GeV bombarding energy, but the 3-GeV data on Bi and Pb interactions illustrate the point. Counter coincidence data⁵² on 2.9-GeV proton interactions with Bi indicated a symmetric mass-yield curve for binary fission peaking at $A \approx 90$ and going to zero at $A \approx 40$ and $A \approx 150$. Normalizing this curve to the cross section for binary fission obtained with mica track detectors⁴⁹ one finds ≈ 5 mb for the peak fission yield (at $A \approx 90$). This accounts for essentially all the radiochemically observed⁷ cross section in this mass range (if one can use the radiochemical data on Pb to compare with the counter data on Bi), whereas at both lower and higher masses appreciable cross sections (~ 3 mb at $A \approx 40$ to 60, 5–6 mb at $A \approx 120$ to 140) are not accounted for by binary fission. Thus it is clear that the mass-yield curve for all processes other than binary fission must have a minimum just in the region of the fission peak. The branch on the high-mass side can be considered as due to high-energy spallation and the magnitude of the integrated cross section is in reasonable agreement with the production cross section for single, unpaired tracks in the mica experiment.

CONCLUSIONS

The results from the present study further substantiate the previous conclusion that different mechanisms predominate in the formation of neutron-excess and neutron-deficient products from the interaction of 28-GeV protons with uranium. The differences of the CD curves for $A \approx 131$, $A \approx 147$, and $A \approx 170$ shown in Fig. 9 clearly demonstrate this point. The mass-yield pattern of the neutron-excess products from this work is remarkably similar to that of low-energy fission as shown in Fig. 2. The apparent constancy of the neutron-deficient yields in the mass range between 143 and 171 is consistent with the yield pattern of a spallation-like process.

Over a wider mass range, however, the picture is more complicated. The area under the mass-yield curve for $50 < A < 160$ can be accounted for

only in part by binary fission and spallation. The contribution due to binary fission, though the exact shape of its mass-yield curve is unknown, corresponds roughly to the integrated area under the broad peak with background of ~ 5 mb at $A = 160$ and background ~ 14 mb at $A = 50$. The spallation, on the other hand, at best can have a constant cross section of ~ 5 mb per mass number over this mass range, leaving at least 0.5 b in cross section not accounted for by either process. In a recent study of energy dependence of recoil properties of products from U in the GeV region, Beg and Porile⁵³ concluded that fragmentation (i.e., emission of a light fragment such as ^{24}Na) is the chief mechanism for the production of neutron-deficient nuclides in the "fission" region at proton energies in excess of 5 GeV. This provides a possibility to account for the cross section of 0.5 b due to "other processes." However, it also makes the distinction between "spallation" and "fragmentation" processes among the neutron-deficient products very difficult without studying their detailed properties. Based on the mass-yield distribution, the contribution of fragmentation should be larger at $A \sim 50$ than at higher masses. Counter experiments designed to look for the partners of light fragments should be most useful in elucidating the mechanism or mechanisms responsible for their formation and their possible connection with the production of nuclides in the "fission product" region.

ACKNOWLEDGMENTS

The authors wish to express their gratitude for assistance from the following: E. Hechtl and R. Zielinsky who helped during the early part of this work; E. Rowland who cheerfully did many of the radioactivity measurements; L. Decker who assisted in the operation of the isotope separator; E. Norton and B. Nine who performed numerous chemical analyses. The helpful and stimulating discussions with J. B. Cumming, J. Hudis, S. Kato, M. L. Perlman, and L. P. Remsberg are most appreciated. The cooperation of the operating staff at the Brookhaven alternating-gradient synchrotron is also hereby acknowledged.

APPENDIX A

Isotope Separation

The feasibility and limitations of the application of radioactive-isotope separation to the study of nuclear reactions have been discussed by Andersson and Rudstam⁵⁴ and also by Klapisch.⁵⁵ The convenience of collecting a large number of nuclides simultaneously and assaying isotopically pure sam-

ples afterwards makes this technique very attractive. However, there are a number of factors to be considered in applying it.

1. *Over-all efficiency.* The typical yield of 0.1 to 1% obtained with the conventional plasma-type ion source is adequate to measure nuclides with half-lives up to a few years and with production cross sections of a fraction of a millibarn in this experiment. The over-all efficiency can be determined after the mass separation by neutron activation of one of the stable isotopes of the carrier added or by assaying the radioactivity of the tracer used.

2. *Separation time.* The shortest half-life that can be studied by this technique is limited by the time required to perform the chemical and mass separations. When a cation-exchange column was used to separate the neighboring rare earths, the shortest time interval between the end of bombardment and the beginning of radioactivity assay on a mass-separated sample was several hours. The isotope with the shortest half-life measured in this work was ^{149}Nd (half-life of 1.7 h). The timing of chemical separations and the duration of mass separation in any particular experiment were determined by the nuclides of interest in that experiment.

3. *Sample collection and cross contamination.* The samples were collected at an empirically determined focal plane. This plane is at an angle of 30° to the ion beam direction at the median position. The collector covers a mass range of $\pm 10\%$ of the median mass. The mass dispersion at mass 150 is 2 cm between adjacent masses. A typical sample size was about 4–5 mm in width and about 2–3 mm in height, depending on the electrostatic potential for the vertical focusing. Cross contamination from the neighboring isotopes was between 0.1% and 1%.

4. *Sputtering loss and saturation loss.* For absolute cross-section measurement, it is important to ascertain that all radioactive isotopes are collected with the same efficiency as is the stable isotope used for over-all yield determination. Obviously any sputtering loss or saturation loss of the yield-determining stable isotope will give erroneous results for the radioactive isotopes. No distinction will be made here as to the mechanisms of the sputtering and saturation processes. In order to determine these effects, the following experiment was performed. Mass separations of a neutron-irradiated ytterbium sample were performed, and varying amounts of the stable isotopes ^{168}Yb (0.135%), ^{174}Yb (31.84%), and ^{176}Yb (12.73%) and of their neutron-capture products $^{169, 175, 177}\text{Yb}$ were collected. The separated stable isotope samples were subjected to neutron irradi-

ation. The radioactivities of ^{169}Yb , ^{175}Yb , and ^{177}Yb from these samples were then compared with the corresponding activities collected in the separator. If there were no losses, the three ratios should be the same and, for sufficiently small amounts collected, this constancy among the ratios was indeed found. For example, with 50-keV ion energy, and about $1\text{-}\mu\text{A}$ Yb^+ beam intensity, no losses occurred up to amounts of $\sim 50\ \mu\text{g}/\text{cm}^2$ collected. Deviations became apparent beyond this point. The amounts of carrier used in each experiment were chosen so as to stay well below this limit.

5. *Mass discrimination.* The widest mass span in a single collection in this work was 8%. The following experiment was carried out to check the mass discrimination effect. A natural ytterbium sample and ^{168}Yb and ^{176}Yb samples obtained from mass separation of natural ytterbium were irradiated with neutrons, and the radiations of ^{169}Yb and ^{177}Yb were assayed. It was found that the ratio of ^{169}Yb to ^{177}Yb radioactivities was 2 to 3% higher in the mass-separated samples than in the natural ytterbium sample. This is in general agreement with the extensive discussion of Anderson and Rudstam.⁵⁴ It should be pointed out, however, that the mass discrimination effect differs in each separation, depending on the specific conditions in the ion source. In any event, the "inverse-square-root-of-the-mass" law⁵⁶ probably serves as a practical upper limit. No mass discrimination correction was applied to any of the measured cross sections.

APPENDIX B

Shell Effects in $Z_A - Z$

The mass data from Ref. 48 were used to evaluate the Z_A values needed in the present work. A least-squares computer program was used to fit the values of mass excess at different Z 's for a given mass number to a parabola and also to determine the charge Z_A corresponding to the minimum of the mass parabola. For even mass numbers, even- Z and odd- Z isobars were fitted to separate parabolas. In principle, when the proton number or the neutron number of the isobars crosses a major shell, the mass data from either side of the shell could be treated separately and different Z_A values were arrived at for the isobars on opposite sides of the shell. For example, Fig. 11 shows a parabola determined by the mass-excess values of $57 \leq Z \leq 62$ for mass 147. The open circles are the mass-excess values taken from Ref. 48. The Z_A value obtained from this parabola is 61.57. For the isobars with $Z \geq 63$, the horizontal deviations of the points from the parabola may

be considered as the shell effects. For each such isobar with a shell effect, a quantity Z_{eff} was evaluated; it is the abscissa of the point on the parabola with the same ordinate (mass excess) as the isobar in question.

The shift from Z to Z_{eff} is the same as the change of Z_A due to the shell effect, and it is more convenient to evaluate Z_{eff} than to use a variable Z_A . For example, it is clear from Fig. 11 that the Z_{eff} for gadolinium is 64.3 instead of 64, and even larger departures of Z_{eff} from the nominal charge values are found for higher Z 's. This is just another way of saying that the Z_A for these higher- Z isobars of mass 147 ($Z > 63$) shifts to lower values gradually as the isobars are crossing the $N=82$ shell. The Z_{eff} values obtained with this procedure for mass 147 are as follows:

Z	62	63	64	65	66	67	68
Z_{eff}	62.01	63.36	64.31	65.44	66.76	68.05	69.26

A note of caution should be added here. Since the mass data available do not always fit the parabolas perfectly, care must be exercised if only mass-excess points on one side and none around the valley of the curve are used to define the parabola. Large uncertainties can be introduced both in the position and the magnitude of the minimum resulting in inaccurate Z_{eff} values.

The Z_A values obtained by fitting the mass parabolas are shown as points on a plot of Z_A/A vs A in

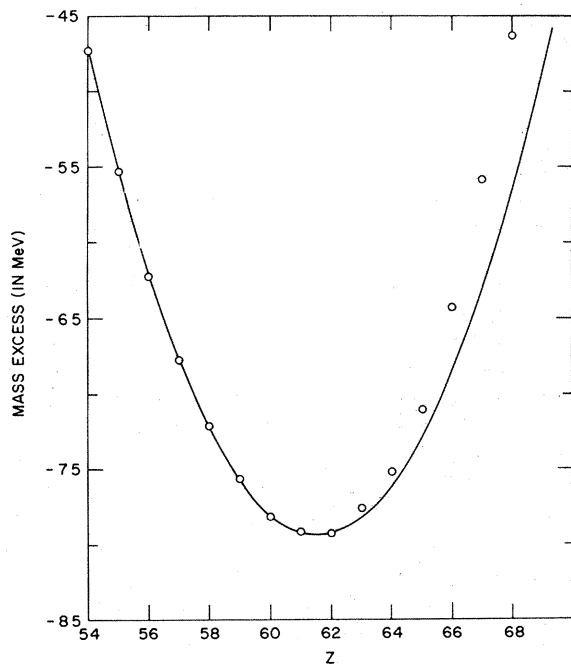


FIG. 11. Mass parabolas for $A = 147$ based on the mass-excess data taken from Ref. 48.

Fig. 12. The Z_A values from Coryell⁵⁷ are shown as solid curves for comparison. Double values of Z_A are shown for several mass numbers. These are values based on mass-excess data on either side of the shell. The scatter of the Z_A 's on the lower branch for $141 \leq A \leq 147$ is a reflection of the difficulty in determining Z_A values when only mass-excess data on one side of the valley were used. Clearly for $A \geq 144$, the values on the upper branch should be used. Since the 82-neutron shell occurs around the valley of the parabolas for $A = 141, 142,$ and 143 , the Z_A values at these masses are rather difficult to determine from either side of the shell as shown by their departures from the general trend of both branches.

APPENDIX C

Transformation of Cs Isotopic Distribution to Charge Dispersion

In converting the isotopic distribution for cesium, shown in Fig. 4, to a CD curve with specified A , it is necessary to transform both the ordinate and abscissa of each data point. The specified value for A is chosen to be 131 because: (a) it is the center of the Cs isotopic distribution (119–144), and (b) there already exists a sizable amount of published recoil and yield data in the vicinity of $A = 131$.

The cross section for each Cs isotope must be corrected according to the appropriate mass-yield change in going from its A value in Fig. 4 to the new value $A = 131$. As mentioned in Sec. IV, the similarity between the mass dependence of neutron-excess yields formed by low-energy fission and by

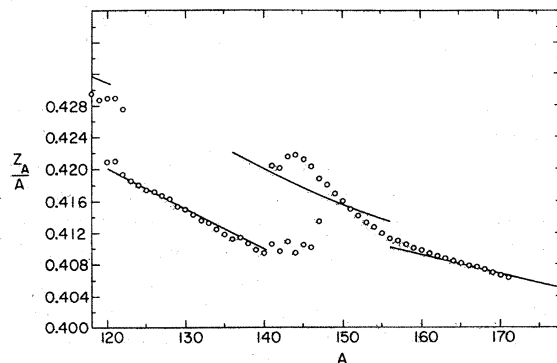


FIG. 12. Z_A values. Points represent Z_A values obtained by fitting the mass-excess data (Ref. 48) to mass parabolas and the solid curves are those of Coryell (Ref. 57). The two sets of points near $A = 120$ were fitted to data below and above the $Z = 50$ shell, respectively. Similarly, the two sets of points for $141 \leq A \leq 147$ correspond to $N < 82$ and $N > 82$, respectively. The additional discontinuity near $A \approx 156$ ascribed by Coryell to a sub-shell at $Z = 64$ is not reproduced in our analysis.

high-energy interactions will be used to advantage in correcting the Cs yields on the neutron-excess side of β stability. For such nuclei with $A \geq 140$ there is little ambiguity in what one means by low-energy fission as can be seen by how little the various sources of data in Fig. 2 differ. The several curves in the figure represent 14.8-MeV-neutron-, and 32- and 150-MeV-proton-induced fission yields normalized to our ^{147}Nd cross section. The curves at 32 and 150 MeV were chosen as defining fission over a reasonable range of low energies. The 14.8-MeV neutron curve is included because it extends to higher masses than the others and illustrates how rapidly the fission yields vanish above $A \sim 155$. The open circles are our data for the neutron-excess mass-yield curve derived directly from those cumulative and independent cross sections listed in Table II which contribute to products with $Z_A - Z > 0$. Figure 2 may now be used to convert the neutron-excess wing, arbitrarily set at $A \geq 137$, of the Cs isotopic distribution into the neutron-excess wing of the CD curve at $A = 131$. At each Cs isotope with $A \geq 137$, the yield is corrected by the relative mass-yield change between $A = 131$ and the cesium mass in question as defined by the two curves in Fig. 2. In this manner, a neutron-excess CD curve wing is developed for each of the two representative low energies selected.

Construction of the extreme neutron-deficient wing of the CD curve at $A = 131$ necessitates a mass-yield curve for neutron-deficient products. Such a distribution may be approximated by subtracting the neutron-excess mass-yield distribution defined by Fig. 2 from the total mass-yield distribution of Fig. 1. The residual distribution for $A \leq 127$ is a reasonable approximation for use in considering only those neutron-deficient cesium isotopes which are not produced by low-energy fission. This residual curve is then applied to the neutron-deficient cesium yields in a manner equivalent to that used for the neutron-excess products.

For the purpose of determining the central portion of the $A = 131$ CD curve from ^{128}Cs to ^{136}Cs , it was assumed that the mass-yield correction changes from one characteristic of neutron-excess products at ^{136}Cs to one characteristic of neutron-deficient products at ^{128}Cs . The procedure adopted was to weight the mass-yield variation linearly from one extreme to the other across the central portion of the distribution. Of course, this procedure does not give a unique definition of this central portion but it provides a smooth connection from one wing of the CD curve to the other and, as it should, leaves the ^{131}Cs yield unchanged and leads to only small corrections for the immediately adjacent points.

*Research performed under the auspices of the U. S. Atomic Energy Commission.

†Present address: Carnegie-Mellon University, Pittsburgh, Pennsylvania 15213.

¹G. Friedlander, L. Friedman, B. Gordon, and L. Yaffe, *Phys. Rev.* **129**, 1809 (1963).

²J. M. Alexander, C. Baltzinger, and M. F. Gazdik, *Phys. Rev.* **129**, 1826 (1963).

³G. Rudstam and G. Sørensen, *J. Inorg. Nucl. Chem.* **28**, 771 (1966).

⁴E. Hagebø, *J. Inorg. Nucl. Chem.* **29**, 2515 (1967).

⁵R. Klapisch, J. Chaumont, J. Jastrzebski, R. Bernas, G. N. Simonoff, and M. Lagarde, *Phys. Rev. Letters* **20**, 743 (1968).

⁶J. Chaumont, Ph.D. thesis, Université de Paris, 1970 (unpublished).

⁷G. Friedlander, in *Proceedings of the Symposium on the Physics and Chemistry of Fission, Salzburg, Austria, 1965* (International Atomic Energy Agency, Vienna, Austria, 1965), Vol. II, p. 265.

⁸N. T. Porile, *Phys. Rev.* **148**, 1235 (1966).

⁹J. A. Panontin and N. T. Porile, *J. Inorg. Nucl. Chem.* **32**, 1775 (1970).

¹⁰E. Hagebø, *J. Inorg. Nucl. Chem.* **32**, 2489 (1970).

¹¹J. Hudis, T. Kirsten, R. W. Stoenner, and O. A. Schaeffer, *Phys. Rev. C* **1**, 2019 (1970).

¹²S. Kaufman, *Phys. Rev.* **129**, 1866 (1963).

¹³G. Friedlander and L. Yaffe, *Phys. Rev.* **117**, 578 (1960).

¹⁴H. Ravn, *J. Inorg. Nucl. Chem.* **31**, 1883 (1969).

¹⁵V. P. Crespo, J. B. Cumming, and A. M. Poskanzer, *Phys. Rev.* **174**, 1455 (1968).

¹⁶R. Brandt, in *Proceedings of the Symposium on the Physics and Chemistry of Fission, Salzburg, Austria, 1965* (International Atomic Energy Agency, Vienna, Austria, 1965), Vol. II, p. 329.

¹⁷K. Bächmann, *J. Inorg. Nucl. Chem.* **32**, 1 (1970); private communication.

¹⁸C. M. Lederer, J. M. Hollander, and I. Perlman, *Table of Isotopes* (Wiley, New York, 1967), 6th ed.

¹⁹Y. Y. Chu, E. M. Franz, and G. Friedlander, *Phys. Rev. C* **1**, 1826 (1970).

²⁰Y. Y. Chu, E. M. Franz, and G. Friedlander, *Phys. Rev.* **175**, 1523 (1968).

²¹L. R. Bunney and E. M. Scadden, *J. Inorg. Nucl. Chem.* **29**, 2497 (1967).

²²H. W. Taylor and A. H. Kukoc, *Nucl. Phys.* **A122**, 425 (1968).

²³Y. Y. Chu, E. M. Franz, and G. Friedlander, *Phys. Rev.* **187**, 1529 (1969).

²⁴J. E. Cline, *Nucl. Phys.* **A96**, 97 (1967).

²⁵R. G. Helmer and L. D. McIsaac, *Phys. Rev.* **143**, 923 (1966).

²⁶E. P. Grigor'ev, A. V. Zolotavin, V. O. Sergeev, M. I. Soltsov, J. Vrzal, N. A. Lebedev, J. Liptak, J. Urbanets, P. P. Dinitriev, N. N. Krasnov, and Yu. G. Sevast'yanov, *Izv. Akad. Nauk SSSR, Ser. Fiz.* **32**, 786 (1968) [transl.: *Bull. Acad. Sci. USSR, Phys. Ser.* **32**, 723 (1968)].

- ²⁷W. R. Daniels and D. C. Hoffman, *Phys. Rev.* **147**, 845 (1966).
- ²⁸B. S. Dzhelepov, P. A. Tishkin, and I. A. Shishelov, *Izv. Akad. Nauk SSSR, Ser. Fiz.* **31**, 205 (1967) [transl.: *Bull. Acad. Sci. USSR, Phys. Ser.* **31**, 184 (1967)].
- ²⁹J. Zylicz, M. H. Jørgensen, O. B. Nielsen, and O. Skilbreid, *Nucl. Phys.* **81**, 88 (1966).
- ³⁰P. J. Karol, *J. Inorg. Nucl. Chem.* **32**, 2817 (1970).
- ³¹D. R. Nethaway and M. C. Missimer, *J. Inorg. Nucl. Chem.* **30**, 15 (1968).
- ³²G. E. Keller, E. F. Zganjar, and J. J. Pinajian, *Nucl. Phys.* **A129**, 481 (1969).
- ³³P. J. Karol, to be published.
- ³⁴S. Reynolds, J. F. Emery, and E. I. Wyatt, *Nucl. Sci. Eng.* **32**, 46 (1968).
- ³⁵C. J. Pariello, E. G. Funk, and J. W. Mihelich, *Bull. Am. Phys. Soc.* **15**, 75 (1970); J. W. Mihelich, private communication.
- ³⁶Y. Y. Chu and J. Reednick, *Phys. Rev. C* **2**, 310 (1970).
- ³⁷G. Kaye, *Nucl. Phys.* **86**, 241 (1966).
- ³⁸G. Kaye, *Nucl. Phys.* **A108**, 625 (1968).
- ³⁹J. B. Cumming, National Academy of Sciences Report No. NAS NS-3107, 1962 (unpublished), p. 25.
- ⁴⁰These calibrations were carried out by use of defining baffles at measured distances from the point sources used. The ¹³¹Cs calibration was kindly performed by Dr. E. Gardner.
- ⁴¹J. B. Cumming, *Ann. Rev. Nucl. Sci.* **13**, 261 (1963).
- ⁴²P. J. Karol, to be published.
- ⁴³Y. Y. Chu, E. M. Franz, and G. Friedlander, to be published.
- ⁴⁴J. R. Grover, *Phys. Rev.* **126**, 1540 (1962); experimental results obtained in Brookhaven National Laboratory by J. Hudis *et al.*
- ⁴⁵D. R. Nethaway, B. Mendoza, and T. E. Voss, *Phys. Rev.* **182**, 1251 (1969).
- ⁴⁶P. C. Stevenson, H. G. Hicks, W. E. Nervik, and D. R. Nethaway, *Phys. Rev.* **111**, 886 (1958).
- ⁴⁷J. J. Hogan and N. Sugarman, *Phys. Rev.* **182**, 1210 (1969).
- ⁴⁸G. T. Garvey, W. J. Gerace, R. L. Jaffe, I. Talmi, and I. Kelson, *Rev. Mod. Phys. Suppl.* **41**, S1 (1969).
- ⁴⁹J. Hudis and S. Katcoff, *Phys. Rev.* **180**, 1122 (1969).
- ⁵⁰L. P. Remsberg, F. Plasil, J. B. Cumming, and M. L. Perlman, *Phys. Rev.* **187**, 1597 (1969).
- ⁵¹G. Rudstam, *Z. Naturforsch.* **21a**, 1027 (1966).
- ⁵²L. P. Remsberg, F. Plasil, J. B. Cumming, and M. L. Perlman, *Phys. Rev. C* **1**, 265 (1970).
- ⁵³K. Beg and N. T. Porile, *Phys. Rev. C* **3**, 1631 (1971).
- ⁵⁴G. Andersson and G. Rudstam, *Nucl. Instr. Methods* **29**, 93 (1964).
- ⁵⁵R. Klapisch, *Ann. Rev. Nucl. Sci.* **19**, 33 (1969).
- ⁵⁶I. Langmuir and K. T. Compton, *Rev. Mod. Phys.* **3**, 191 (1931).
- ⁵⁷C. D. Coryell, *Ann. Rev. Nucl. Sci.* **2**, 305 (1953).

Experiments on Parity Nonconservation in Nuclear Forces II. Gamma Transitions in ²⁰³Tl and ⁷⁵As†

J. C. Vanderleeden,* F. Boehm, and E. D. Lipson
California Institute of Technology, Pasadena, California 91109
(Received 6 July 1971)

The circular polarization P_γ of the 279-keV γ ray in ²⁰³Tl and the 401-keV γ ray in ⁷⁵As has been measured using a Compton polarimeter and a current-measuring technique. The result for ²⁰³Tl is $P_\gamma = (2 \pm 5) \times 10^{-6}$. For ⁷⁵As evidence for a nonzero circular polarization, $P_\gamma = (-0.6 \pm 0.2) \times 10^{-4}$, is found. The role of the electron-capture bremsstrahlung in the case of ⁷⁵As is discussed.

I. INTRODUCTION

In a recent paper by Vanderleeden and Boehm¹ (hereafter referred to as I) we reported on measurements of the circular polarization of γ rays from unpolarized radioactive nuclei. The cases investigated were the 482-keV transition in ¹⁸¹Ta [$P_\gamma = -(3.9 \pm 1.2) \times 10^{-6}$], and the 396-keV transition in ¹⁷⁵Lu [$P_\gamma = (6.3 \pm 1.0) \times 10^{-5}$]. The results agree with recent findings of others,² and they contribute to confirming the existence of a weak, parity-nonconserving (PNC) nuclear potential, as predicted by the current-current theory of the weak interaction.³ The evidence for the PNC po-

tential is further strengthened by the results of other recent experiments, namely (i) the detection of a $P_1(\cos\theta)$ term in the angular distribution of γ rays emitted by ¹¹⁴Cd nuclei, following capture of polarized neutrons,⁴ and (ii) the observation⁵ of a parity-forbidden α decay between the 8.8-MeV 2^- state in ¹⁶O and the 0^+ ground state in ¹²C.

These findings can be compared with calculations of the strength of the PNC admixtures, \mathcal{F} , in the nuclear states (see the references cited in the review articles by Henley and Blin-Stoyle⁶). The uncertainty in \mathcal{F} is largely due to the approximations in the nuclear-structure calculations, as well as to the particular choices of the form of the